The Plant Cell, Vol. 28: 875–891, April 2016, www.plantcell.org

Three-Dimensional Visualization of the Tubular-Lamellar Transformation of the Internal Plastid Membrane Network during Runner Bean Chloroplast Biogenesis

Łucja Kowalewska,[a] Radosław Mazur,[b] Szymon Suski,[c] Maciej Garstka,[b] and Agnieszka Mostowska[a,1]

[a] Department of Plant Anatomy and Cytology, Faculty of Biology, University of Warsaw, 02-096 Warsaw, Poland
[b] Department of Metabolic Regulation, Faculty of Biology, University of Warsaw, 02-096 Warsaw, Poland
[c] Laboratory of Electron Microscopy, Nencki Institute of Experimental Biology, Polish Academy of Sciences, 02-093 Warsaw, Poland

ORCID IDs: 0000-0002-4090-6291 (Ł.K.); 0000-0003-3615-1911 (R.M.); 0000-0001-7141-505X (M.G.); 0000-0003-4109-5125 (A.M.)

Chloroplast biogenesis is a complex process that is integrated with plant development, leading to fully differentiated and functionally mature plastids. In this work, we used electron tomography and confocal microscopy to reconstruct the process of structural membrane transformation during the etioplast-to-chloroplast transition in runner bean (*Phaseolus coccineus*). During chloroplast development, the regular tubular network of paracrystalline prolamellar bodies (PLBs) and the flattened porous membranes of prothylakoids develop into the chloroplast thylakoids. Three-dimensional reconstruction is required to provide us with a more complete understanding of this transformation. We provide spatial models of the bean chloroplast biogenesis that allow such reconstruction of the internal membranes of the developing chloroplast and visualize the transformation from the tubular arrangement to the linear system of parallel lamellae. We prove that the tubular structure of the PLB transforms directly to flat slats, without dispersion to vesicles. We demonstrate that the grana/stroma thylakoid connections have a helical character starting from the early stages of appressed membrane formation. Moreover, we point out the importance of particular chlorophyll-protein complex components in the membrane stacking during the biogenesis. The main stages of chloroplast internal membrane biogenesis are presented in a movie that shows the time development of the chloroplast biogenesis as a dynamic model of this process.

INTRODUCTION

Chloroplast biogenesis is a complex process that is essential for plant ontogenesis. It involves changes in gene expression together with the transcriptional and translational control of both nuclear and plastid genes. These genes can be regulated by anterograde and retrograde signals, the synthesis of necessary lipids and pigments, the import and routing of the nucleus-encoded proteins into plastids, protein-lipid interactions, the insertion of proteins into the plastid membranes, and the assembly into functional complexes (Vothknecht and Westhoff, 2001; Baena-González and Aro, 2002; Kota et al., 2002; Stern et al., 2004; López-Juez, 2007; Waters and Langdale, 2009; Solymosi and Schoefs, 2010; Adam et al., 2011; Pogson and Albrecht, 2011; Ling et al., 2012; Jarvis and López-Juez, 2013; Lyska et al., 2013; Belcher et al., 2015; Börner et al., 2015; Dall'Osto et al., 2015; Ling and Jarvis, 2015; Rast et al., 2015; Sun and Zerges, 2015; Yang et al., 2015). Chloroplast biogenesis is highly integrated with cell and plant development, especially with photomorphogenesis (Pogson et al., 2015), and is controlled by cellular and organismal regulatory mechanisms such as the ubiquitin-proteasome system (Jarvis and López-Juez, 2013). Although biogenesis of chloroplasts has been a subject of investigations for many years, the correlation of simultaneous changes at the structural, biochemical, and functional level was described only recently when time-dependent models of chloroplast biogenesis for bean (*Phaseolus vulgaris*) and pea (*Pisum sativum*) were described (Rudowska et al., 2012).

The development of chloroplasts up to the stage of etioplasts often takes place when seedling growth proceeds without light. Etioplasts contain characteristic structures known as prolamellar bodies (PLBs) that have tubules joined together in a regular network and have a special paracrystalline symmetry. Together with prothylakoids (PTs), flattened porous membranes, PLBs are precursors of the chloroplast thylakoid membranes. PLBs are observed under natural growing conditions when the first stages of seed germination proceed under the ground and are not artificial laboratory phenomena (Solymosi et al., 2007; Solymosi and Schoefs, 2010; Vitányi et al., 2013). The paracrystalline structure of PLBs can differ depending on the species and the conditions of PLB crystallization. All types of paracrystalline arrangements have an exceptionally high surface-to-volume ratio (Gunning, 2001). The formation of etioplasts in darkness, which have a characteristic paracrystalline PLB, and their transformation upon exposure to light has been documented since the 1960s (Gunning, 1965, 2001; Mostowska, 1986a, 1986b; Solymosi and Schoefs, 2010), but the spatial arrangement of these changes is still not known.

Despite 60 years of studies, the true organization of the paracrystalline membranes in three dimensions has remained unclear. Cubic membranes other than PLBs were described in different

[1] Address correspondence to mostowag@biol.uw.edu.pl.
The author responsible for distribution of materials integral to the findings presented in this article in accordance with the policy described in the Instructions for Authors (www.plantcell.org) is: Agnieszka Mostowska (mostowag@biol.uw.edu.pl).
www.plantcell.org/cgi/doi/10.1105/tpc.15.01053

biological systems, especially in stressed conditions or virally infected cells (Almsherqi et al., 2006, 2009; Deng et al., 2010). However, this widespread phenomenon is poorly understood due to having limited tools available to depict periodic arrangements of cubic membranes having a lattice constant in the range of 50 to 1000 nm (Chong and Deng, 2012). This makes electron tomography (ET) an extremely valuable tool to study the nonlamellar membrane configurations in cells. Complimentary investigation to mathematically describe the spatial arrangement as a triply periodic minimal surface and compare the 2D transmission electron microscopy (TEM) images with the 2D projections of these theoretical models has been quite useful (Deng and Mieczkowski, 1998). However, the ET technique is still required to confirm any cubic membrane configuration predicted by the above direct template matching technique (Chong and Deng, 2012). The connections of the cubic structures with the adjacent tubular or lamellar arrangements, and thus the spatial changes of the local topology within the paracrystalline structure, are difficult to properly predict. An alternative method applied to precisely determine PLB tubule dimensions as well as the unit cell size, is small-angle x-ray scattering. Small-angle x-ray scattering performed on isolated maize (*Zea mays*) PLBs confirmed their paracrystalline structure, with the diamond cubic lattice being the most abundant type. The unit cell size was 78 nm (Selstam et al., 2007). However, the dimensions of isolated structures and those in sliced tissue, i.e., in situ performed by the ET technique, are difficult to compare. In similar studies, ET was used to determine the cubic structure of the inner mitochondrial membrane morphology in amoeba (*Chaos carolinens*) upon starvation (Deng et al., 1999).

The paracrystalline nature of PLBs is thought to be due to the aggregation of a complex containing protochlorophyllide (Pchlide), light-dependent protochlorophyllide oxidoreductase (LPOR), and NADPH (Pchlide-LPOR-NADPH) (Ryberg and Sundqvist, 1982). The spatial structure can be clarified by studying the mechanism of aggregation of such complexes and their interactions with the membrane lipids (Mysliwa-Kurdziel et al., 2013). Although PLB tubules contain more monogalactosyldiacylglycerol than PTs that facilitate cubic phase structure formation, both PLBs and PTs are composed from the same types of lipids: monogalactosyldiacylglycerol, digalactosyldiacylglycerol, sulfoquinovosyldiacylglycerol, and phosphatidylglycerol. Thus, it appears that the lipid composition is not a critical factor and that proteins appear to play an important role (Selstam, 1998). It is known that integral membrane proteins have a stabilizing effect on the bilayer membrane even in the presence of purified nonbilayer lipids (Rietveld et al., 1987). This is probably due to a strong interaction between the hydrophobic region passing through the membrane and the hydrophobic tails of the lipid molecule (Taraschi et al., 1982). Proteins are also considered to be important in vitro for transforming nonbilayer lipids into the lamellar structure (Simidjiev et al., 2000). The role of the large pigment-protein complex Pchlide-LPOR in the formation of PLB membranes with a cubic phase structure is probably due to the ability of this pigment-protein complex to form an oligomer and to anchor the LPOR protein into the membrane (Selstam, 1998). Moreover, the proper composition of carotenoids in the PLB membrane can play an important role in the formation and maintenance of its paracrystalline structure (Park et al., 2002).

PLBs contain two spectral forms of the Pchlide-LPOR complexes with absorption maxima at ~640 and 650 nm (Selstam et al., 2002). These two Pchlide forms are photoconvertible. An analysis of low-temperature fluorescence (77K) spectra has revealed one more type of Pchlide: the nonphotoconvertible form Pchlide 628-633 (Böddi et al., 1998). The longer wavelength forms are bound to PLBs, while this shorter wavelength form, unbound to LPOR, is mainly found in PTs. In addition to LPOR, PLBs contain enzymes of the chlorophyll and carotenoid biosynthesis pathways, enzymes of the Calvin cycle, and proteins involved in photosynthetic light reactions (subunits of ATP synthase, the oxygen-evolving complex, cytochrome b_6f, plastocyanin, and ferrodoxin-NADPH oxidoreductase) and other proteins necessary during photomorphogenesis with the exception of the core subunits and the antenna complexes of the two photosystems (von Zychlinski et al., 2005; Kleffmann et al., 2007; Blomqvist et al., 2008; Adam et al., 2011).

Upon illumination, the photomorphogenic process called greening or deetiolation takes place and etioplasts develop into chloroplasts (Ryberg and Sundqvist, 1982; Mostowska, 1986a; Von Wettstein et al., 1995). During this process, PLBs begin to both disperse and transform, and Pchlide is phototransformed to chlorophyllide (Chlide). In angiosperms, LPOR, the major protein of PLB membranes, is responsible for the NADPH-dependent reduction of Pchlide to Chlide during illumination (Selstam et al., 2002). Recently it was shown using isolated wheat (*Triticum aestivum*) PLBs that the photoreduction was followed by the disruption of the PLB lattice and the formation of vesicles around the PLBs. Data on isolated PLBs obtained by TEM were correlated with atomic force microscopy results (Grzyb et al., 2013). The release of Chlide from a Chlide-LPOR complex leads to the degradation of the paracrystalline PLB structure (Selstam et al., 2002).

In the case of meristematic tissues, chloroplast development proceeds mainly from a proplastid (Charuvi et al., 2012). In this case, the thylakoid membrane is formed by invaginations of the inner chloroplast envelope. In the differentiated chloroplast, however, the vesicle-based transport system dominates (Rast et al., 2015). If a proplastid develops into an etioplast in darkness but later the PLB transformation takes place upon illumination, the structural changes differ from those in meristematic tissues. In this case, the transfer system for the newly synthesized lipids and proteins into the forming thylakoids can be similar to that occurring during the direct development of a proplastid into a chloroplast (Rast et al., 2015). However, it is still not clear whether the degrading PLB transforms into thylakoids continuously or through the formation of vesicles (Rosinski and Rosen, 1972; Adam et al., 2011; Grzyb et al., 2013; Pribil et al., 2014).

Eventually, the tubular system of PLBs transforms into a linear system of lamellae arranged in parallel to each other, and the first grana appear as overlapping thylakoids. Finally, fully developed chloroplasts have the internal membrane system differentiated into stacks of appressed thylakoids and nonappressed regions with grana margins as well as stroma lamellae linking grana together. The structure of mature thylakoids is determined by the lipid composition and arrangement of chlorophyll-protein (CP) complexes, hierarchically organized in supercomplexes and

megacomplexes, and spatially segregated (Dekker and Boekema, 2005; Kouřil et al., 2012; Rumak et al., 2012). The main component of the appressed regions is photosystem II (PSII), forming together with extrinsic antennae light-harvesting complex II (LHCII) supercomplex LHCII-PSII, while the light-harvesting complex I-photosystem I supercomplex (LHCI-PSI) is localized in nonappressed thylakoids (Danielsson et al., 2004, 2006). The organization, composition, dynamics, and structural rearrangements of the developed photosynthetic apparatus of higher plants under changing light conditions have been examined with high-resolution microscopic techniques and by spectroscopic and biochemical methods (Nevo et al., 2012; Janik et al., 2013; Garab, 2014; Jensen and Leister, 2014; Pribil et al., 2014).

Spatial models of the thylakoid membrane architecture were created with the help of ET in the case of fully mature higher plant chloroplasts (Shimoni et al., 2005; Daum et al., 2010; Austin and Staehelin, 2011) and *Chlamydomonas reinhardtii* chloroplasts (Engel et al., 2015). The most probable model of thylakoid membrane organization is based on the pioneering results of Paolillo (1970). This is a modified helical model of chloroplast membranes that shows an imperfect regularity (Mustárdy et al., 2008; Daum et al., 2010; Daum and Kühlbrandt, 2011) and a large variability in size of the junctional connections between the grana and stroma thylakoids (Austin and Staehelin, 2011).

Although the 3D view of the overall structure of chloroplasts has been already presented based on confocal laser scanning microscopy (CLSM) (Rumak et al., 2010, 2012) and on 3D models of the thylakoid membrane architecture of mature chloroplasts using ET (Shimoni et al., 2005; Daum et al., 2010; Austin and Staehelin, 2011), a 3D membrane visualization during the etioplast-to-chloroplast transition can give important developmental information. Without this full 3D information, it is not possible to understand the process of the transformation of the membrane structure during the chloroplast biogenesis.

In this article, we establish the spatial 3D structure of successive stages of runner bean (*Phaseolus coccineus*) chloroplast biogenesis by ET and by CLSM. We reconstructed the paracrystalline structure and the membrane connections within the PLB and the gradual transformation from a tubular arrangement to the linear one during the greening process. Moreover, we present the early stages of grana formation, especially the character of the grana-stroma thylakoid connections. We reconstruct the spatial structure of the internal plastid membrane using ET, with the aid of CLSM in later stages. This enables visualization and, thus, an understanding of the membrane connections during the key stages of chloroplast biogenesis. We correlate the 3D structure of PLBs and of the developing bean thylakoid network with the formation of CP complexes.

The results of our studies show that the transformation of PLBs consists of the untwining of tubules from the PLB structure in a continuous process. The tubular structure of the prolamellar body transforms directly, without dispersion into vesicles, into flat slats that eventually, in a continuous way, form grana. We demonstrate that grana membranes, from the beginning of their formation, associate with stroma thylakoids in a helical way.

RESULTS

Spatial Model of Chloroplast Biogenesis

To determine the spatial structure of successive stages of bean chloroplast biogenesis during three day/night cycles, both CLSM and ET were used. Previous results from ultrastructural analysis indicated that starting from 8-d-old etiolated plants, chloroplast development proceeds synchronously in all plastids (Rudowska et al., 2012).

To establish the sequence of structural changes of the thylakoid network during chloroplast biogenesis, we followed the process of biogenesis step-by-step from the paracrystalline structure of PLB to the stacked membranes observed in the ultrastructure of bean chloroplasts. For the ET analysis, seven stages of plastid internal membrane arrangements were selected during the photomorphogenesis, as described in Methods (Supplemental Figure 1).

We focused, on one hand, on areas of membrane connections within tightly organized tubular PLB structure and grana thylakoids, and on the other hand, on areas of loosely organized structure with transforming PLBs with newly formed thylakoids. 3D modeling was performed from the stage of paracrystalline structure of PLB to the stage of reorganization into first appressed thylakoids and formation of more developed grana.

Reconstruction of the very early stages of chloroplast development by CLSM was not reliable due to the small dimensions and lack of red chlorophyll fluorescence in early developmental stages. Because of this, the images of the etioplast internal membranes obtained with CLSM were not comparable with relevant structures on electron micrographs. Moreover, the lipophilic dye [$DiOC_{18}(3)$] that was used in these early stages did not incorporate uniformly into the tight paracrystalline and transforming PLB membranes, causing imaging artifacts. Therefore, spatial models obtained from CLSM were used only in the two latest analyzed stages of biogenesis, when the chlorophyll autofluorescence of PSII was sufficiently stable and the dimensions of chloroplasts were large enough.

Stage 1.0: Paracrystalline Prolamellar Body

Eight-day-old etiolated bean leaves have etioplasts with characteristic paracrystalline prolamellar bodies, as was already shown by us and other researchers (Rudowska et al., 2012). Based on Gunning and Steer (1975), bean etioplast PLB is of a closed type with hexagonal symmetry of the tubule arrangement. The tetrahedrally branched basic tubular units form a typical wurtzite (a zinc iron sulfide mineral) lattice. For a better comparison between the PLB structure and the theoretical model of a hexagonal lattice, we chose perpendicular sections of the closed-type PLB for ET analysis (Supplemental Figure 2).

We found that the structure of the PLB was a regular tetrahedral arrangement of tubular connections within the PLB (Figure 1). Such a composite tomographic image stack was obtained by superimposing reconstructed parallel slices, such as the one shown in Figure 1A. The volume of the PLB (Figure 1B) and isosurface visualization of the 3D reconstruction of paracrystalline PLB membranes was generated (Figure 1C) with the help of Imaris microscopy image processing and analysis software. In Figures 1C and 1D, the PLB volume together with the first layer of the PLB

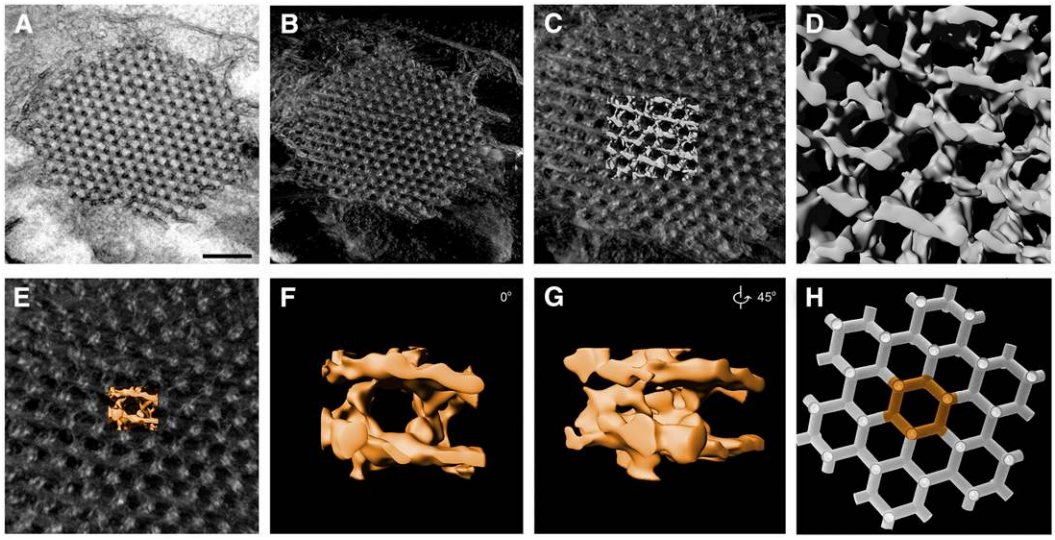

Figure 1. Model of the Paracrystalline Tubular Structure of a PLB after 8 d of Etiolation (Stage 1.0).

(A) Middle layer of the tomography stack.
(B) Volume of the 3D reconstructed PLB.
(C) and **(D)** Isosurface visualization with magnification, showing a regular paracrystalline network. The image in **(D)** shows a magnification of the light-colored surface area in **(C)**.
(E) Isosurface view of a single PLB unit (orange).
(F) and **(G)** Magnification of a PLB unit viewed from two different angles (orange).
(H) Theoretical model of a single layer of the PLB network (3ds max).
Bars = 250 nm

is visible. For better visualization of the PLB network, we highlight a single unit (orange) of the PLB together with the rendered volume (Figure 1E). An enlargement of the isosurface of one unit is shown (Figure 1F) together with its side view (Figure 1G). In Figure 1H, the theoretical model created with the help of 3ds max software showing the arrangement of inner plastid membranes within the prolamellar body is displayed.

Stage 1.1: Irregular Prolamellar Body

After 1 h of illumination, the regularity and the symmetry of the PLB were lost. The structure of the PLB became irregular and PLB membranes became rearranged (Figure 2). The 3D array of branched tubes in the PLB became dissociated and the characteristic tetrahedral network was no longer visible, and all units lost regular connections with each other. A composite tomographic slice image was obtained by superimposing reconstructed parallel slices representing the spatial structure of an irregular PLB, and this composite image is shown in Figure 2A. The volume (Figure 2B) and isosurface (Figures 2C to 2H) of an irregular PLB was rendered with the help of Imaris software. Already at this stage PLB membranes both within the PLB (Figures 2E to 2H) and in its marginal regions (Figure 2D) had given rise to flat stromal slats at the periphery of the PLB that were seen as porous PTs. PTs were tightly connected with the degrading PLB that were radially spreading from the PLB margins (Figure 2C). In Figures 2C and 2D, the isosurface of the irregular PLB together with the outer layer of the PLB is visible. Upon magnification, the PTs emerging from the degrading PLB are seen as flat slats (Figure 2D). For better visualization of the transformation from tubular elements to slats, a single unit of a degrading PLB net (lime green) is shown from various directions (Figures 2E to 2H).

We strongly emphasize that ET enabled the visualization of slat arrangements during transformation and untwining of PLB nodes. This was not possible in traditional electron microscopy.

Stage 1.2: Remnants of PLB and Numerous Prothylakoids

After 2 h of illumination, only remnants of the PLB were observed (Figure 3). A composite tomographic slice image was obtained by superimposing reconstructed parallel slices of remnants of the PLB and porous PTs connected with them (Figure 3A). The area of interest was drawn on every slice with the help of 3DMOD software (Figure 3B, the middle slice in the stack). We reconstructed a particular area of chloroplast membranes focusing on connections between the remnants of the PLB and the PTs. This model was superimposed on a TEM image for better visualization of the region of interest (blue) (Figures 3C and 3D). In Figures 3E to 3G, slat-like images of PTs are presented from different angles. From these models, we could observe that the membranes that were remnants of the PLB had a continuous character, as opposed to the porous PT membranes that were tightly connected with the former (Figures 3E to 3G). Both types of membrane were slat-like and not tubule-like structures. At this stage of chloroplast biogenesis, the inner membranes were arranged in parallel to the long chloroplast axis.

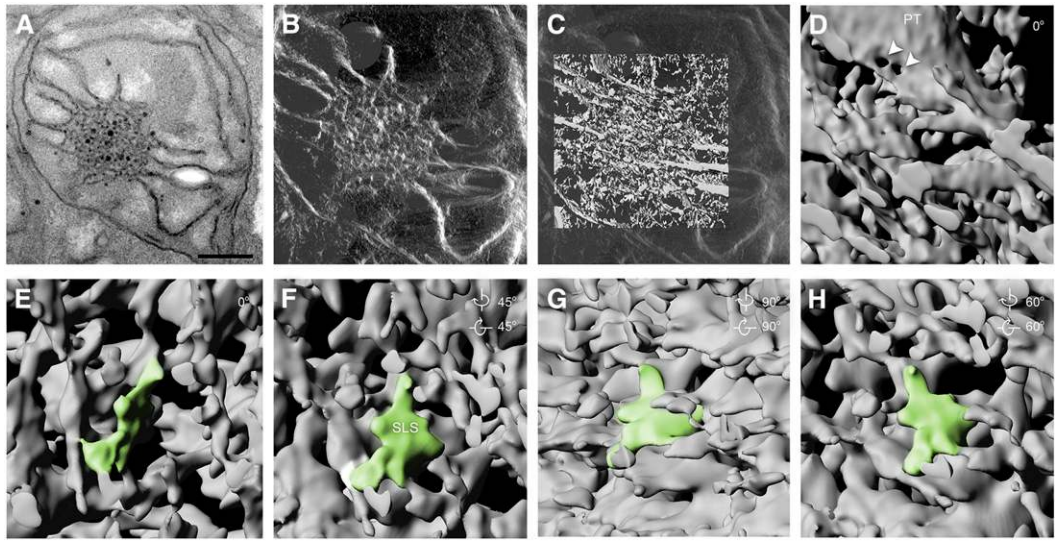

Figure 2. Model of the PLB Irregular Structure after 1 h of Illumination (Stage 1.1).

(A) Middle layer of the tomography stack.
(B) Volume of the 3D reconstructed irregular PLB.
(C) and **(D)** Isosurface visualization with magnification. Note the lamellar character of porous (arrowheads) prothylakoids at the PLB edges. The image in **(D)** shows a magnification of the part of the light-colored surface area in **(C)**.
(E) to **(H)** Magnification of the irregular PLB network viewed from four different angles showing a portion of a degraded PLB unit (lime green) forming sheet-like structures (SLS).
Bars = 500 nm

Stage 1.4: Parallel Prothylakoids

After 4 h of illumination, there were no more remnants of PLBs in the bean chloroplasts (Figure 4). A composite tomographic slice image was obtained by superimposing reconstructed parallel slices of chloroplasts at this stage of development (Figure 4A). A selected area of membranes was drawn with the help of 3DMOD software (Figure 4B, middle slice from the stack). A model of the area of interest was superimposed on a TEM image for better visualization (purple) (Figures 4C and 4D). In Figures 4E to 4G, slat-like models of porous PTs are shown after rotation and presented from different angles. Such models enabled the visualization of the parallel arrangement of PTs and the local connections between them. The PTs had a slat-like and porous character and some of them had split in a dichotomous manner (Figures 4E to 4G).

Stage 1.8: First Stacked Membranes

After 8 h of illumination, the first stacked membranes were observed (Figure 5). A composite tomographic slice image was obtained in a similar way as before (Figure 5A). Interesting areas of thylakoid membranes, especially of stacked membranes and their connections to unstacked ones, were drawn using 3DMOD software (Figure 5B, middle slice from the stack). A model of the area of interest was superimposed on the TEM image (Figures 5C and 5D). In Figures 5E to 5H, models of the first stacked membranes are shown after magnification and are presented from different angles. These models revealed that the appressed thylakoids (light yellow) were no longer porous but had continuous membranes in the stacked region. From our constructed model, we learned that the PTs (yellow) remained still porous, although to a lesser extent than at earlier stages. In this model, each stacked membrane was connected to a single split PT. This dichotomous splitting existed only locally where a PT joined with both the upper and lower stacked membrane. The PT membrane connected with the stacked region not in parallel but at an angle in the range of 18° to 33°.

Stage 2.0: Small Grana

At the beginning of the second day of the experiment (Figure 6), small grana stacks were observed (stage 2.0). A composite tomographic slice image was obtained in a similar way as for the other stages of biogenesis (Figure 6A). Grana thylakoids (GTs) and stroma thylakoids (STs) connected with them were drawn using the 3DMOD software (Figure 6B, middle slice from the stack). A small grana model was superimposed on the TEM image for a better visualization of the region of interest (Figures 6C and 6D). The model shows GTs (light green) arranged in parallel and no longer porous STs (green) connected with them (Figure 6E). In Figures 6F to 6I, the models of GTs and STs are shown from different angles. Every modeled ST was connected with two adjacent GTs (Figures 6F and 6G). The STs were connected with the stacked region at an angle of ~20°.

As mentioned previously, a CLSM study was performed for the two latest stages of chloroplast biogenesis. The density of the red

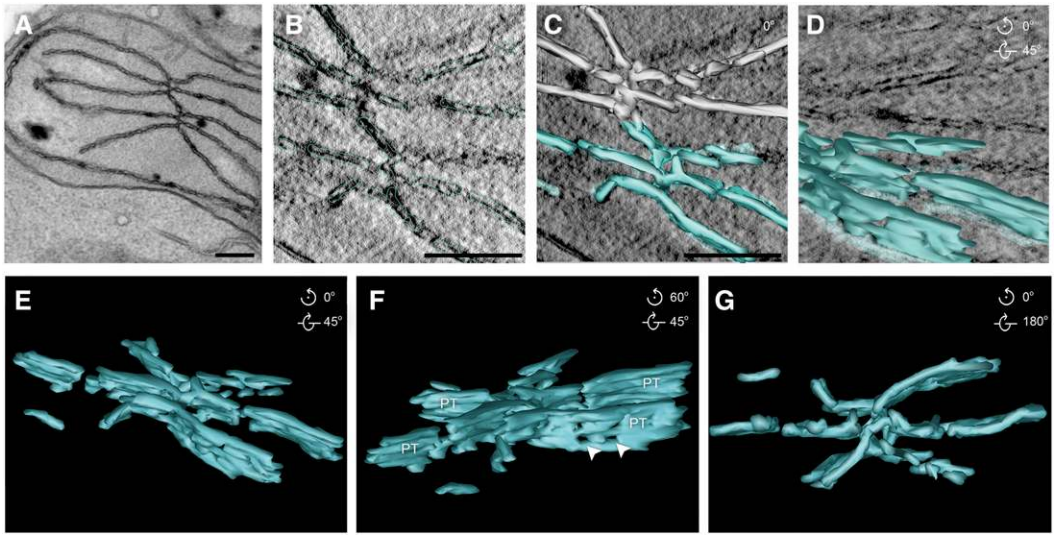

Figure 3. Model of Degraded PLB Structure with Numerous PTs in Plastid Stroma after 2 h of Illumination (Stage 1.2).

(A) Middle layer of the tomography stack.
(B) Magnification of the modeled region (blue)
(C) and **(D)** Surface model (blue) embedded in the middle TEM layer viewed from two different angles.
(E) to **(G)** Surface visualization from three different angles showing the radial arrangement of porous (arrowheads) prothylakoid structures.
Bars = 200 nm

chlorophyll fluorescence spots in a CLSM image showed the distribution of the appressed thylakoids (grana) in the chloroplast (Supplemental Figure 3). There was no visible regularity of the appressed thylakoid distribution (Supplemental Figure 3A) that correlated with the TEM pictures. Also, 3D models of the computer generated isosurface of chlorophyll fluorescence (Supplemental Figures 3B to 3D) confirmed the lack of regularity of grana location within a chloroplast. The red fluorescence originated from the LHCII-PSII supercomplexes, dimers, and monomers as well as from LHCII trimers that were not bound and

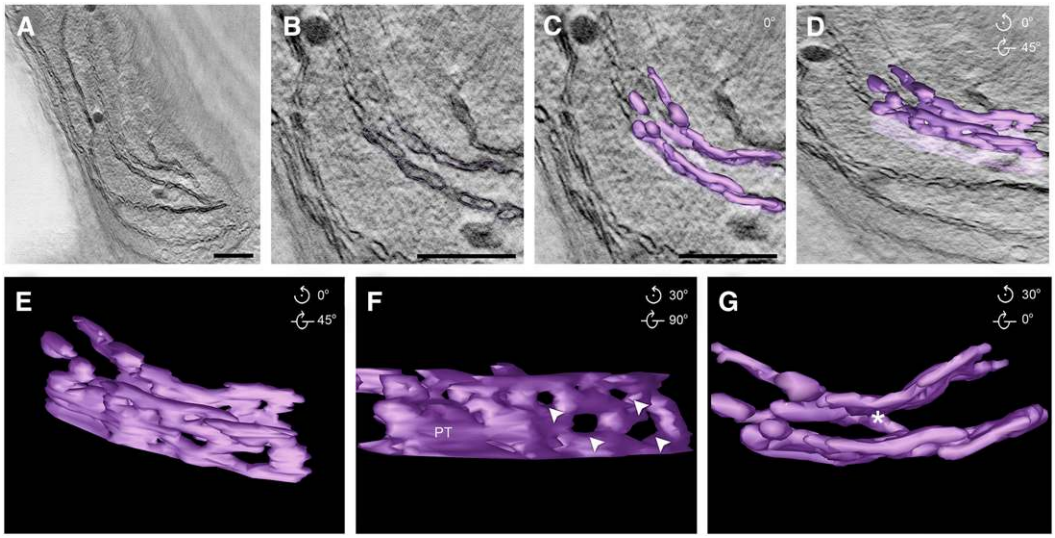

Figure 4. Model of PTs Loosely Arranged in Plastid Stroma after 4 h of Illumination (Stage 1.4).

(A) Middle layer of the tomography stack.
(B) Magnification of the modeled region (purple).
(C) and **(D)** Surface model (purple) embedded in the middle TEM layer viewed from two different angles.
(E) to **(G)** Surface visualization from three different angles showing parallel porous (arrowheads) prothylakoid structures, with a locally visible dichotomous split of a prothylakoid (asterisk).
Bars = 200 nm

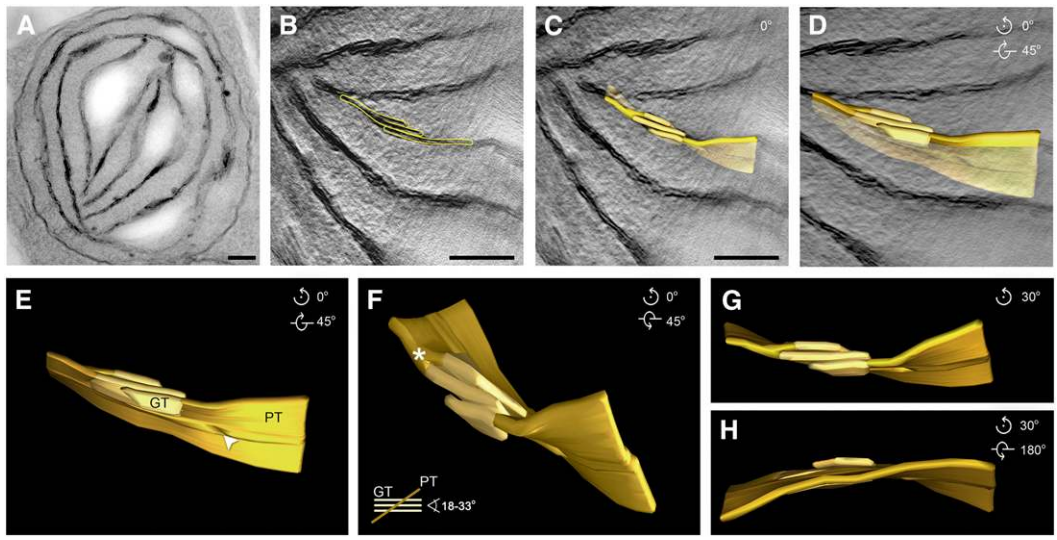

Figure 5. Model of the First Stacked Membranes after 8 h of Illumination (Stage 1.8).

(A) Middle layer of the tomography stack.
(B) Magnification of the modeled region (yellow).
(C) and **(D)** Surface model embedded in the selected TEM layer viewed from two different angles.
(E) to **(H)** Surface visualization from four different angles showing three layers of a nonporous thylakoid stack (light yellow) and associated porous (arrowhead) prothylakoid membrane (yellow) connected with the stacked region at an angle in the range of 18° to 33° with a locally visible splitting of a prothylakoid (asterisk).
All bars = 250 nm

localized in grana (Mehta et al., 1999). Selective images of PSI and PSII in plant chloroplasts in situ have shown that they are spatially separated from each other; however, the majority of the fluorescence signals originating from PSI overlap with those from PSII (Hasegawa et al., 2010). Thus, in the case of CLSM images of bean chloroplasts, the LHCI-PSI complexes can be located both in red and dark areas, but the LHCII-PSII and LHCII trimers are located in red fluorescence regions only.

Stage 3.3: More Developed Grana

During the third day (stage 3.3), chloroplasts with grana more developed than in the previous stage, containing numerous thylakoids, were observed (Figure 7). A composite tomographic slice image was obtained as in the previously analyzed stages (Figure 7A). The region of interest was drawn using the 3DMOD software (Figure 7B, middle slice from the stack). A model of the granum (light navy) with connected STs (navy) was superimposed on the TEM image (Figures 7C and 7D). In Figures 7E to 7I, the model is shown from different angles to visualize direct connections of STs with GTs. The complexity of these connections can be observed. Some STs were associated with two neighboring GTs as in the previous stage and were connected at an angle of ~18° (Figures 7E and 7F); ST can also split in a dichotomous manner and connect with both the adjacent GT and the next GT in the other slice (left bottom ST; Figures 7F and 7H). Additionally, we saw that the ST in the area of our model could connect with only one GT, as was observed at the top and bottom of the granum (Figure 7G). This shows that the junctional slits created by the connections between GTs and STs can be of different widths, as was also reported by Austin and Staehelin (2011) for the thylakoid network of well developed chloroplasts of mature plants.

For this stage, the CLSM analysis was also performed. The distribution of chlorophyll autofluorescence (Supplemental Figure 4) visible in CLSM changed drastically in comparison to the earlier stage of grana formation. Red spots corresponding to grana were uniformly distributed within the chloroplast (Supplemental Figure 4A). 3D models of the computer-generated isosurface of chlorophyll fluorescence confirmed the regular distribution of grana that is characteristic of a mature chloroplast (Rumak et al., 2010) (Figures 4B to 4D). However, the size of chloroplast at this stage of biogenesis was much smaller (~3 μm) than the 6-μm chloroplasts found in mature plants.

Based on the TEM sections of numerous developmental stages and on the reconstruction of the membrane transformation in 3D during the seven stages of chloroplast biogenesis, we proposed a 2D theoretical model (Figure 8) of the membrane changes. The proposed theoretical model of membrane rearrangements taken together with the 3D models allowed us to create a dynamic model of chloroplast development, which is presented as a movie (Supplemental Movie 1).

Summarizing the structural part of our work, we have presented in detail the models obtained by ET that describe several stages in chloroplast development: the PLB paracrystalline lattice and its transformation; the untwining of tubules from the PLB structure as a continuous process; the change of their conformation to stromal flat slats, even inside a degrading PLB; and eventually the

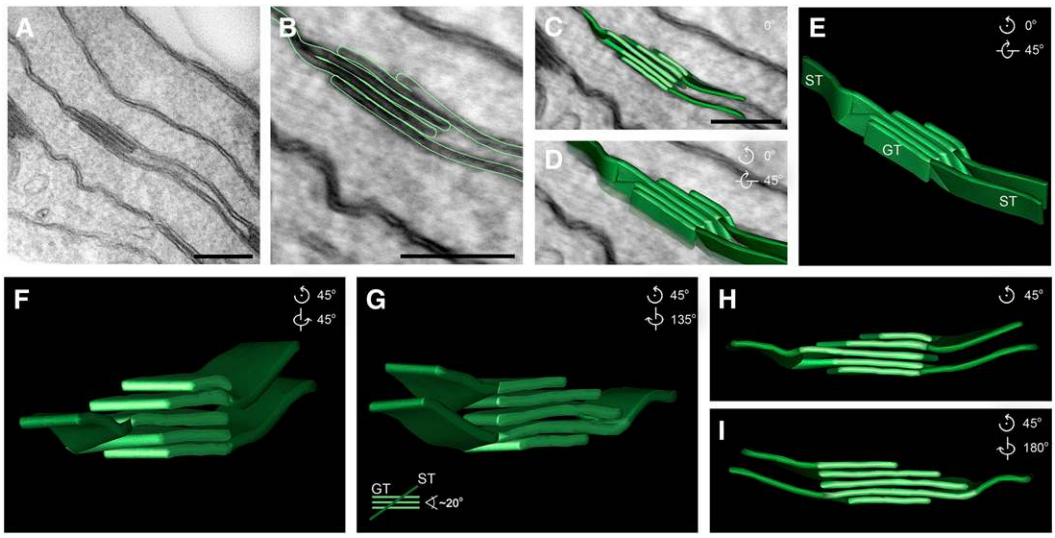

Figure 6. Model of Small Grana at the Beginning of the Second Day of the Experiment (Stage 2.0).

(A) Middle layer of the tomography stack.
(B) Magnification of the modeled region (green).
(C) and **(D)** Surface model embedded in the selected TEM layer viewed from two different angles.
(E) to **(I)** Surface visualization from five different angles showing five grana thylakoid layers (light green) arranged in parallel. These grana are directly connected with three nonporous stroma thylakoids (green). The stroma thylakoids are connected with a stacked region at an angle of ~20°.
Bars = 200 nm

formation of a well developed grana with STs linked to GTs at an angle of ~18°. Additional models of the two latest of the analyzed stages of chloroplast biogenesis obtained by CLSM demonstrated the 3D details of the architecture of the early grana distribution.

Quantitative EM Analysis of Grana Formation during Biogenesis of the Chloroplast

To quantify the grana formation process during chloroplast biogenesis, we measured the diameter, height, and number of membrane layers of the grana (Supplemental Table 1) as described in Methods. Grana lateral irregularity (GLI) is defined as the coefficient of variation (the ratio of the SD to the mean) of membrane diameters within the granum. The GLI in stages 2.0 and 3.3 was lower in comparison to stage 1.8, both for grana with different numbers of membranes (Supplemental Table 2) and for subgroups with the same membrane count in the grana (Supplemental Table 3). When comparing all the data from stages 2.0 and 3.3, the difference in the GLI value was statistically insignificant (Supplemental Table 2). However, for the four-membrane grana, the irregularity of grana was lower in stage 3.3 (Supplemental Table 3). During chloroplast biogenesis, the stacking repeat distance (SRD) value decreased continuously in subsequent developmental stages (Supplemental Table 4). Spearman's rank correlations between the height of the granum and the number of stacked membranes increased in subsequent stages ($1.8 < 2.0 < 3.3$) (Supplemental Table 5), confirming a gradual increase of the membrane compaction in the growing grana, thus lowering the SRD value. Moreover, the dominating direction of grana enlargement differed between successive stage-to-stage transitions. During the transition from the first stacked membranes (stage 1.8) to small grana (stage 2.0), there was a tendency for membrane expansion in the lateral rather than vertical direction, while during the transition from stage 2.0 to 3.3, the tendency was reversed (Supplemental Table 6 and Supplemental Figure 5).

Formation of CP Complexes during Biogenesis of the Chloroplast

The association of chlorophyll species with photosynthetic proteins and the formation of the CP complexes in isolated intact etioplasts and in developing bean chloroplasts were analyzed from data obtained by the application of complementary methods: low-temperature fluorescence emission and excitation spectroscopy, mild-denaturing electrophoresis, and immunodetection of proteins associated with PSII (Figure 9).

When normalized to the same area, steady state 77K fluorescence emission spectra reveal the relative contribution of specific species to the overall fluorescence pattern. As shown in Figure 9A, two bands (at 630 and 653 nm) were observed in etiolated bean seedlings. The first one corresponds to free Pchlide species, whereas the latter is related to the Pchlide-LPOR-NADPH complex in PLB (Schoefs and Franck, 2008; Adam et al., 2011, and references therein). After 1 h of illumination, the 653-nm band completely disappeared and a new red-shifted band at ~679 nm was observed. This indicates a decline of Pchlide associated with LPOR complex, despite the significant band, still present, corresponding to free Pchlide (Schoefs and Franck, 2008; Gabruk et al., 2015). The corresponding excitation spectra, reflecting

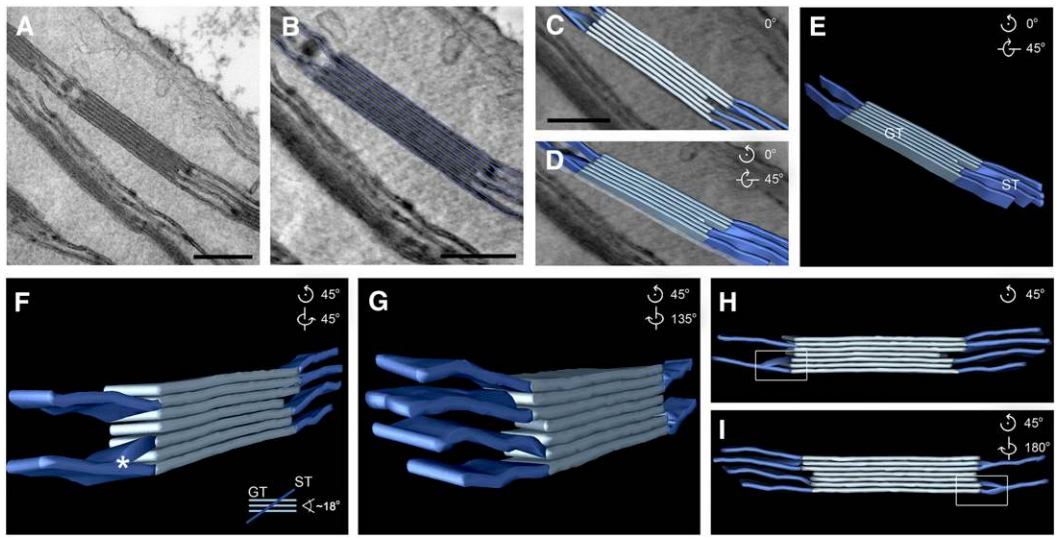

Figure 7. Model of More Developed Grana Visible during the Third Day of Day/Night Growth (Stage 3.3).

(A) Middle layer of the tomography stack.
(B) Magnification of the modeled region (green).
(C) and **(D)** Surface model embedded in the selected TEM layer viewed from two different angles.
(E) to **(I)** Surface visualization from five different angles showing a very regular parallel arrangement of grana thylakoid layers (light navy) associated with six stroma thylakoids (navy).
(F) Splitting of the bottom stroma thylakoid (star).
(G) Stroma thylakoids are connected with two neighboring grana thylakoids at an angle of ~18°.
(H) and **(I)** A particular stroma thylakoid is split in two and connected with the adjacent grana thylakoid **(H)** and with the next grana thylakoid in another slice **(I)**, as shown inside the small white rectangles.
Bars = 200 nm

relative energy transfer from the absorbing pigments to the emitting chlorophyll species (Figure 9B), showed a Chlide/chlorophyll *a* related band at ~440 nm (Gabruk et al., 2015), suggesting energy transfer to Chlide/chlorophyll *a* species only. Simultaneous structural investigation by mild denaturing electrophoresis (Figure 9D) and immunodetection (Figure 9E) did not reveal the presence of either CP complexes or proteins associated with PSII.

Illumination for 2 h (Figure 9A) caused a shift of a red band to 683 nm and formation of a new wide far-red band at ~724 nm. These changes indicated further degradation of Pchlide-LPOR complexes with simultaneous appearance of the core complexes. The far-red band is related to the spectrum of the PSI core complex (Klimmek et al., 2005; Rumak et al., 2012). The presence of the 683-nm band in the emission spectra (Figure 9A) and the excitation band at 437 nm corresponding solely to light harvesting by chlorophyll *a* (Figure 9B) is a counterpart of the CP43/CP47 spectra seen previously (Andrizhiyevskaya et al., 2005; Casazza et al., 2010). The immunodetection pattern of the stage 1.2 sample showed traces of CP43 and a lack of visible CP47, D1, and D2 bands (Figure 9E), indicating that, after 2 h of illumination, the CP43 inner antenna was the dominating CP complex. In the emission spectrum of the stage 1.4 sample, besides the 683-nm band, a shoulder at ~691 nm appeared (Figure 9A) with simultaneous significant increase of the 470-nm chlorophyll *b* band in the excitation spectrum (Figure 9C). The 691-nm band originates from the PSII core and CP43 intrinsic antenna bound with chlorophyll *a* (Rumak et al., 2012). The 683-nm band can be related to LHCII complexes containing both chlorophylls *a* and *b* apart from the CP47 complex (Rumak et al., 2012). Immunoblot analysis revealed only traces of CP43 and Lhcb2 in the stage 1.4 sample (Figure 9E), suggesting that these proteins create the first CP complexes related to PSII. However, no green bands assigned to more organized CP complexes were resolved by mild denaturing electrophoresis (Figure 9D). This suggests that in the first parallel PT membranes (stages 1.2 and 1.4), the arrangement of rare CP complexes differs substantially from that in mature thylakoids.

Eight hours of seedling illumination radically changed the spectroscopic and electrophoretic pattern. The emission and excitation spectra (Figures 9A and 9C) are very similar in shape to those observed in thylakoids isolated from mature leaves. The red band revealed two separate maxima at 683 nm both from trimers and monomers of LHCII and CP43, while the 691-nm band corresponds to the PSII core (Rumak et al., 2012). The appearance of the 728-nm band suggests incorporation of the LHCI antenna complexes into membranes (Klimmek et al., 2005; Rumak et al., 2012). The excitation spectrum indicates the presence of both chlorophyll *a* and *b* (Figure 9C). Furthermore, the D1 core protein was the only nonvisible protein associated with LHCII/PSII (Rumak et al., 2012) (Figure 9E). Mild denaturing electrophoresis (Figure 9D) revealed only traces of LHCI-PSI, LHCII-PSII supercomplexes (upper bands), and LHCII trimers (middle band) (Rumak et al., 2012). These data indicate an early phase of the CP organization in

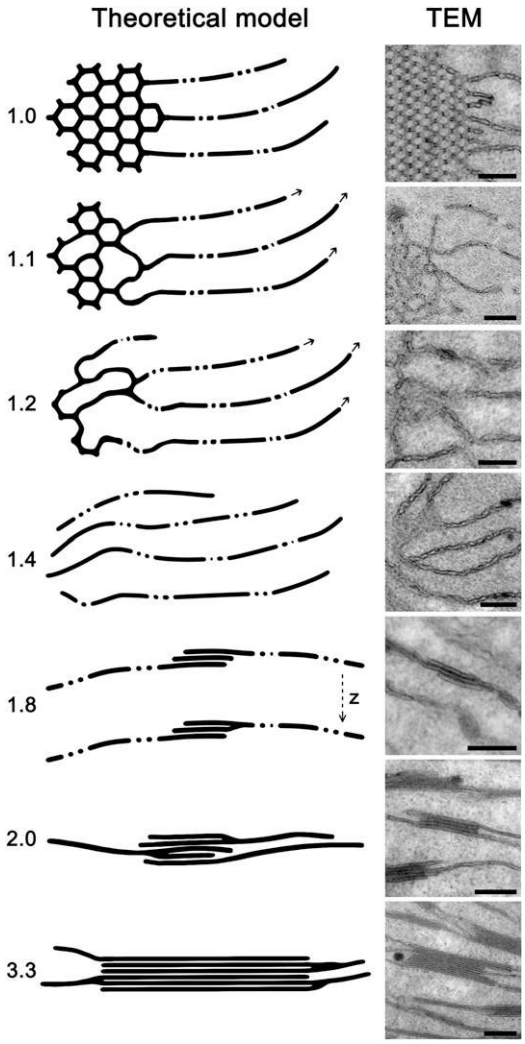

Figure 8. Theoretical 2D Models of Subsequent Stages of Inner Chloroplast Membrane Transformations.

Membrane transformations during the etioplast-chloroplast transition induced by illumination, with the corresponding developmental stages illustrated (left panels) and visualized by TEM (right panels). The theoretical models show membrane connections at a selected depth on the *z* axis of the chloroplast volume. Bars = 200 nm.

the lateral plane of the thylakoid membranes, probably restricted to smaller dispersed microdomains (Rumak et al., 2010). The ordered arrangement of LHCII and of LHCII-PSII complexes stabilizes the structure of grana stacks (Rumak et al., 2010), but due to the still limited number of complexes, the interaction between adjacent membranes occurs only in a small group of membranes (Figure 5).

The spectra and electrophoretic patterns obtained for developing chloroplasts isolated from 2- and 3-d-old seedlings (Figure 9) do not differ qualitatively from those of mature thylakoids (Rumak et al., 2012). Sharp bands in the spectra (Figures 9A and 9C) suggest precise arrangements of pigments in the CP complexes. The total number of supercomplexes and LHCII trimers and monomers (Figure 9D) was less than in mature thylakoids (Garstka et al., 2005; Rumak et al., 2012) and corresponded to the grana seen in 2- and 3-d-old plants (Figures 6 and 7). A simple relationship was also observed between the gradual accumulation of the LHCII apoproteins (Figure 9E) and an increase of the grana stacks (Supplemental Table 1).

DISCUSSION

This work describes in detail the spatial 3D reconstruction of the paracrystalline arrangement of PLB and its gradual transformation from a tubular to a linear system during the greening process. The structural changes during the early stages of chloroplast biogenesis have been visualized.

The PLB is a paracrystalline membrane structure typical for angiosperm etioplasts (Gunning and Steer, 1975). The most basic structures of the PLB lattice correspond in their symmetry to two crystal forms of zinc sulfide in which tetrahedrally branched units join together in 3D networks of hexagons. The first, wurtzite type, is that of the hexagonal close-packed structure. Hexagons of the neighboring crystallographic planes (above and below) form a hexagonal prism. The second lattice type corresponding to zinc-blende (sphalerite) is a cubic close-packed structure. In this lattice type, successive planes of hexagonal rings are displaced half a ring with respect to one another. These two types are the most common among the basic structures of PLBs. Other crystallographic lattices, e.g., pentagonal dodecahedron, open or centric type, can also be present. Two lattice structures can be present in one PLB, resembling polycrystals. In addition, other combinations and configurations of the PLB lattice can be found (Gunning, 2001). The only type of PLB lattice observed in the etiolated bean plastids was of the wurtzite-type hexagonal prism (Figure 1). However, the type of lattice might be in different under growing conditions.

Different kinds of such highly organized and complex cubic or tubule-reticular structures evolve not only from plastid inner membranes or smooth endoplasmic reticulum but also directly from plasma membranes, nuclear envelopes, mitochondrial cristae systems, and Golgi complexes and are ubiquitous in many different cell types under specific environmental conditions (for a review of cubic membrane occurrence in biological systems, see Almsherqi et al., 2009). A hexagonal paracrystalline membrane arrangement of endoplasmic reticulum, structurally similar to a PLB, was observed in cytoplasm of compactin-resistant Chinese hamster ovary cells that were grown for 72 h in stressed conditions in the presence of 40 μM compactin. Compactin is a competitive inhibitor of 3-hydroxy-3-methylglutaryl CoA reductase, the rate-limiting enzyme in cholesterol synthesis. This confirms the possibility of creating such unique structure via a different combination of lipids and proteins in organisms that are evolutionarily distant (Chong and Deng, 2012).

Although the structural aspects of chloroplast biogenesis have been the subject of research over the last 30 years (Ryberg and Sundqvist, 1982; Mostowska, 1986a, 1986b; Von Wettstein et al., 1995; Gunning, 2001; Adam et al., 2011), the character of the transformation of the tubular paracrystalline PLB structure to a linear thylakoid arrangement was not observed as a continuous

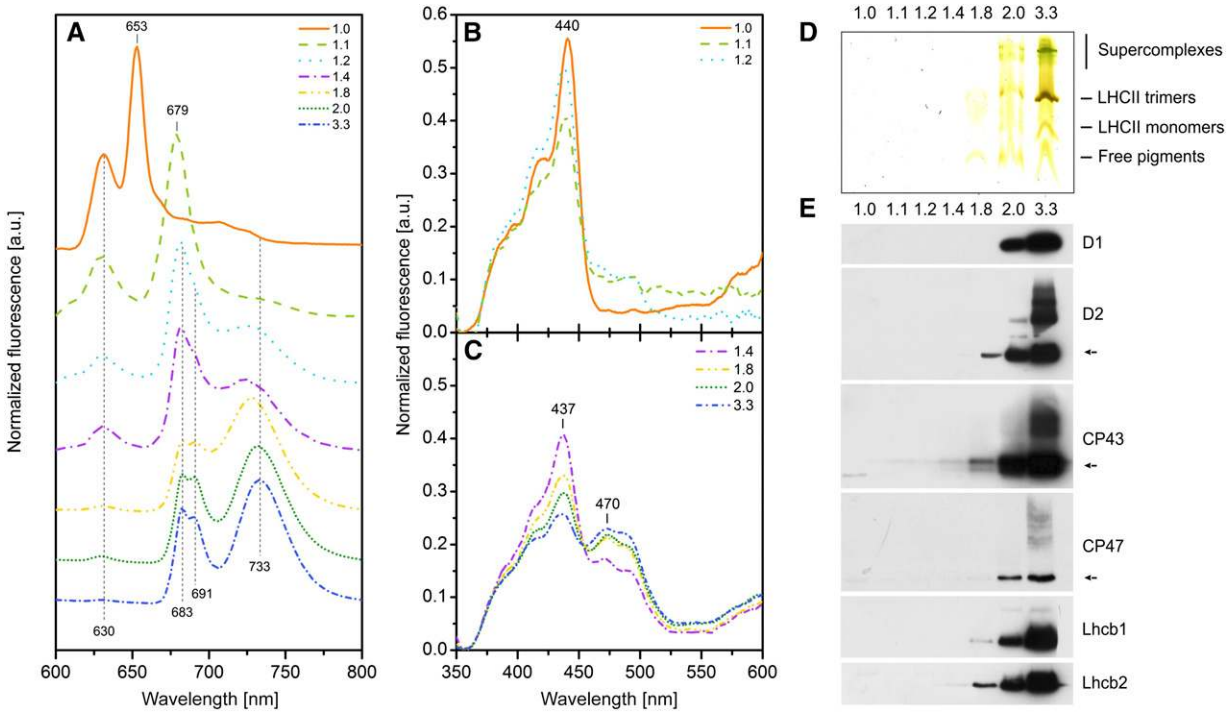

Figure 9. Analysis of CP Complexes during the Biogenesis of Chloroplasts.

(A) Low-temperature (77K) fluorescence emission spectra (excitation at 440 nm) of isolated intact bean etioplasts and developing chloroplasts from subsequent developmental stages as shown in the key at upper right.

(B) and **(C)** Low-temperature (77K) fluorescence excitation spectra obtained from emission at 653 nm (stage 1.0), 680 nm (stage 1.1), or 683 nm (stages 1.2 to 3.3) (line styles are the same as in **[A]**).

(D) Mild denaturing green gel electrophoresis of CP complexes.

(E) Immunodetection analysis of PSII core (D1, D2, CP43, and CP47) and extrinsic antenna (Lhcb1 and Lhcb2) proteins. All measurements were repeated at least three times; all spectra presented were normalized to equal area under the curve.

process. Other authors have described the disintegration of PLBs into vesicles upon illumination, in particular as a disruption of isolated paracrystalline wheat PLBs into vesicles that rearrange into strands dispersed through the stroma (Klein et al., 1964; Grzyb et al., 2013) and also as vesicle formation on the surface of the PLB together with a transition of the tubular network into lamellae (Solymosi et al., 2006). Such observations were not confirmed by our results using ET on bean leaf sections. Even in the 1970s, a PLB transformation to porous primary thylakoids was described as a rearrangement of existing membranes and pores of PTs as relics of the lattice spacing of the PLB (Gunning and Steer, 1975). We have demonstrated that the paracrystalline structure of the PLB transforms directly to lamellar structures that are porous from the beginning. This direct transformation can explain the presence of so many photosynthetic proteins in the PLB in the darkness, which results in photomorphogenic growth upon illumination (Blomqvist et al., 2008). Already at the beginning of the untangling of the paracrystalline network, tubules were transformed into porous flat slats even in the midst of the degrading PLB (Figure 2).

In Chlamydomonas, the pyrenoid, which is considered to be a nucleation center for thylakoid maturation, is penetrated by thylakoid tubules. In other algal chloroplasts, translation membranes surround or cut across the pyrenoid. Although our study deals with the chloroplasts of an angiosperm, which differ from the chloroplasts of algae, it can be speculated that, during the thylakoid biogenesis of the angiosperm chloroplast, PLBs with connected PTs and the pyrenoid of the algae chloroplast can play a similar structural role (Rast et al., 2015). Regularity of PLBs in the bean plastids (Figure 1) was observed simultaneously with the band at 653 nm corresponding to the Pchlide-LPOR-NADPH complex (Figure 9A) (Abdelkader et al., 2007; Blomqvist et al., 2008; Schoefs and Franck, 2008; Adam et al., 2011, and references therein). The transformation of PLBs observed after 1 h of illumination was seen as a loss of regular connections through interconnecting tubules (Figure 2). At the same time that the nodes of the paracrystalline network vanished, the fluorescence of Pchlide-LPOR-NADPH complex was no longer observed (Figure 9A).

In some other species growing in the day/night cycle, e.g., in pea, a partial reconstruction of the PLBs after the dark period during the chloroplast differentiation was observed (Abdelkader et al., 2007; Schoefs and Franck, 2008; Rudowska et al., 2012). It is not clear why such a reconstruction of PLBs in bean plastids (i.e., a reconstruction of the cubic phase after the dark period) was not observed. Fourier transform infrared spectroscopy analysis showed that the protein/lipid ratio (i.e., the average protein

density) was higher in bean than in pea thylakoids, which might limit the protein diffusion within bean thylakoid membranes and their plasticity (Rumak et al., 2010). This might be the reason why bean PLB reconstruction does not take place.

During the first hours of illumination, the flat slats emerging directly from the bean PLB visualized by ET remain porous (Figures 2 to 4) until the first neighboring thylakoids overlap (Figure 5). Formation of the first parallel or partially overlapping membranes (Figure 5) coincides with the appearance of the first CP complexes. Appearance of the extrinsic antennae follows the core complexes, but the arrangement of the CP complexes is much different from the final structure observed in mature thylakoids (Figure 9). Such immaturity of the stacked membrane arrangement in stage 1.8 was also reflected in the highest SRD value, which then gradually declined during the biogenesis process (Supplemental Tables 4 and 5). Stacking of thylakoids in order to form grana interconnected by nonstacked thylakoids is a complicated process that includes protein-protein and protein-lipid interactions in the lateral and vertical plane of the membranes as well as thermodynamic changes inside the chloroplast environment (Jia et al., 2014). Vertical appression of adjacent membranes is associated with an increase of van der Waals attractions and a decrease of the electrostatic and hydration repulsion (Chow et al., 2005). The appression process is feasible due to lateral separation of CP complexes: PSI, which has a large protrusion at the stroma-facing surface, is segregated to nonappressed thylakoids (Chow et al., 2005), while LHCII-PSII and LHCII are localized in appressed membranes by a self-organized process (Kirchhoff et al., 2007; Rumak et al., 2010).

Commonly accepted models point out the essential role played by the amount of LHCII in grana formation, based on the observation of LHCII-deficient barley (*Hordeum vulgare*) mutants, on liposomes with incorporated LHCII, and on pea thylakoid membranes with a removed stromal-exposed N-terminal segment of LHCII (Nevo et al., 2012). In this last model, a positively charged N-terminal segment of LHCII in one membrane interacts with a negatively charged stromal surface of the opposite LHCII trimer (Standfuss et al., 2005; Daum et al., 2010). Recently, however, the significance of LHCII-PSII supercomplexes and the LHCII trimer arrangement in grana membranes has been emphasized (Kim et al., 2009; Kouřil et al., 2012; Tietz et al., 2015). The contact between stacked adjacent membranes is made by the stromal surfaces of polypeptides of supercomplexes, mainly LHCII trimers, PSII core, and minor antennae (Daum et al., 2010). The adjacent membranes are separated by a stromal gap (Kim et al., 2005), whereas supercomplexes form more or less ordered arrays in appressed grana thylakoids (Kirchhoff et al., 2008; Daum et al., 2010). The size of the lumen space of the thylakoids depends on the interaction between oxygen evolving complexes of the PSII from opposite lamellae (Anderson et al., 2008; Kirchhoff et al., 2008). Furthermore, the participation of other proteins such as PsbS and CURT1 has been considered (Goral et al., 2012; Pribil et al., 2014).

In a developing chloroplast after 8 h of illumination (stage 1.8) (Figure 5), the first small stacks appear at the same time as the first ordered structures of LHCII and LHCII-PSII (Figure 9). The close association of the membranes causes a coalescence of perforations, while the neighboring stroma lamellae still remain porous (Figure 5). The ET model of the 1.8 stage (Figure 5) revealed that even in the case of the first stacked membranes, the STs associate with GTs in a helical way forming an angle of 18° to 33°. This pattern of spatial structure is similar to that in the fully developed grana where the observed angle was ~20° (Mustárdy et al., 2008; Austin and Staehelin, 2011; Daum and Kühlbrandt, 2011). The formation of gradually more complicated grana structure observed in the 2- and 3-d-old seedlings (Figures 6 and 7) correlates not only with the increase of LHCII abundance but also with arrangement of supercomplexes (Figure 9). In these phases of development, the pores in thylakoids are no longer observed neither in grana nor stroma (Figures 6 and 7).

The interpretation of tomographic, fluorescence, and electrophoretic data taken together suggest that both the accumulation of CP complexes and their arrangement in supercomplexes influence the formation of appressed membranes during chloroplast biogenesis. Development during illumination changes the grana size and the appressed thylakoid distribution (Supplemental Figures 3 and 4). The increased size of the grana can occur through enlargement in lateral and vertical directions. We have shown that the expansion of the grana membrane changes direction from lateral to vertical during illumination (Supplemental Table 6 and Supplemental Figure 5). Upon illumination, not only do the grana become more regularly distributed, but also the irregularity of the grana structure expressed by the GLI parameter decreases (Supplemental Tables 1 to 3). The spatial organization of thylakoids inside the chloroplast of higher plants varies between species and mutant lines (Kim et al., 2009; Rumak et al., 2012). These effects might depend on the qualitative and quantitative properties of CP complexes and their arrangements, as demonstrated on 3D CLSM models of developed pea and bean chloroplasts (Rumak et al., 2012). Thus, the composition of the thylakoid microdomains and the lateral separation of photosystems might be another mechanism involved in grana formation (Rumak et al., 2010). Despite this diversity, the general lamellar organization is similar, as shown by the broad plasticity of the system (Pribil et al., 2014). The structural ET analyses performed on thylakoids of mature spinach (*Spinacia oleracea*), tobacco (*Nicotiana tabacum*), pea, and *Arabidopsis thaliana* chloroplasts, and also our results performed on developing bean chloroplasts, confirm the presence of a helical grana arrangement of GTs connected with STs by staggered membrane protrusions (Daum et al., 2010; Austin and Staehelin, 2011). We showed that the arrangement of spiraling STs and stack forming exactly parallel GT membranes originates very early during grana formation (Figure 5). The next stages (Figures 6 and 7) follow this helical pattern of grana arrangement, emphasizing its importance for the structural mechanism of grana thylakoid assembly. Thus, our observation serves as a general pattern of thylakoid biogenesis.

Our study has provided the spatial models of chloroplast biogenesis that have allowed the reconstruction of the 3D structure of internal membranes of a developing chloroplast. It also allowed us to visualize their interconnections and their transformation from a tubular arrangement to a linear one. We show that the tubular structure of the prolamellar body transforms directly into flat slats, without dispersion to vesicles, a matter that has been the subject of debate. We also demonstrated that the helical character of the grana-stroma thylakoid connections is observed from the beginning of the formation process of the stacked membrane

arrangement. Moreover, we described the importance of particular CP complex components in the membrane appression during biogenesis. The main stages of the biogenesis of the plastid internal membrane network are presented by a dynamic model in the associated movie (Supplemental Movie 1).

METHODS

Plant Material and Growth Conditions

Runner bean (*Phaseolus coccineus* cv Eureka) seeds were germinated on Petri dishes in darkness. After 7 d of germination, the seedlings were transferred to 3-liter perlite-containing pots with nutrient solution containing 3 mM $Ca(NO_3)_2$, 1.5 mM KNO_3, 1.2 mM $MgSO_4$, 1.1 mM KH_2PO_4, 0.1 mM $C_{10}H_{12}N_2O_8FeNa$, 5 μM $CuSO_4$, 2 μM $MnSO_4 \times 5\ H_2O$, 2 μM $ZnSO_4 \times 7\ H_2O$, and 15 nM $(NH_4)_6Mo_7O_{24} \times 4\ H_2O$, pH 6.0 to 6.5, in a climate-controlled room (18°C) for the next 8 d (etiolation). The first samples were collected under photosynthetically inactive dim green light directly after etiolation. Then, the light was switched on and the growing conditions were changed to 21°C/18°C (day/night) with photosynthetic active radiation of 40 μmol photons $m^{-2}\ s^{-1}$ during a 16-h-light/8-h-dark photoperiod at a relative humidity of 60 to 70%. Leaf samples were taken at selected collection times during the 3 d of the experiment (Supplemental Figure 1). Sample selection was based on our preliminary experiments, which indicated that these moments correspond to significant steps in chloroplast biogenesis. Samples from each stage of development were taken for various measurements as required: TEM, ET, CLSM, as well as for the fluorescence measurements and at the same time for electrophoresis and immunoblotting. The sample collection times corresponding to the structural stages are labeled according to the number of days and hours of illumination (e.g., 1.2 denotes 2 h of illumination during the first day of illuminated growth). Seven stages from 3 d of greening were analyzed by ET: paracrystalline prolamellar body (stage 1.0); irregular prolamellar body (stage 1.1); remnants of PLB and numerous prothylakoids (stage 1.2); parallel prothylakoids (stage 1.4); first stacked membranes (stage 1.8); from the second day, small grana (stage 2.0); and from the third day, more developed grana (stage 3.3). Additionally, the last two stages of the day/night growth were also analyzed via CLSM.

TEM

Samples from each developmental stage were taken for the TEM analysis. Material cut from the middle part of the leaf was fixed in 2.5% glutaraldehyde in 0.05 M cacodylate buffer (pH 7.4) for 2 h, washed in buffer, and postfixed in 2% OsO_4 at 4°C in 0.05 M cacodylate buffer for ~12 h. We used glutaraldehyde as a preferred primary fixative in protocols for the preservation of paracrystalline arrangements (Chong and Deng, 2012). Immediately after that, the specimens were dehydrated in a graded acetone series and then embedded in epoxy resin (Epon; Sigma-Aldrich). Polymerization was performed at 50°C for 3 d. The material was cut on a Leica UCT ultramicrotome into 70-nm sections. Specimens on nickel formvar-coated grids with 100 mesh were stained with uranyl acetate and lead citrate and examined with the JEM 1400 electron microscope (Jeol) of the Nencki Institute of Experimental Biology of the Polish Academy of Sciences, Warsaw.

Grana Measurements and Statistical Analysis

Based on the TEM micrographs of the 1.8, 2.0, and 3.3 developmental stages, we measured the diameter, height, and number of membrane layers for 100 grana in each of the analyzed stages using ImageJ software (Abramoff et al., 2004). From these data, we calculated the SRD, which is defined as the distance between the adjacent partition gaps in the stacks (Kirchhoff et al., 2011). The analysis of the changes in grana regularity was based on these data. We also introduced a parameter named GLI as a measure of grana stack irregularity. The GLI value is defined as the coefficient of variation (the ratio of the SD to the mean) of membrane diameters within the granum. The minimum theoretically possible GLI value of 0 would be attained for grana consisting of membranes of the same diameter; the larger the irregularity (diameter fluctuations), the larger the GLI value. The relative variation gives a better measure of irregularity than an absolute one for many reasons; in particular, chord error caused by measurements of random cross sections of grana stacks influences the absolute values more than the relative ones.

An analysis of the measurement protocol drew attention to an ambiguity in the definition of the ending positions of stacked membranes that led us to omit two-membrane stacks from the statistical analysis. This was in order to eliminate a potential source of artifacts in the membrane diameter calculation.

To compare the GLI values between stages, we found the interval estimates (at 95% confidence level) of the GLI ratios for pairs of stages. Whenever possible, we also performed such a comparison separately for classes of grana consisting of the same number of membranes. This was to avoid possible artifacts due to a potential dependence of the diameter measurement on the number of membranes. To compare the vertical compactness between stages, we found the interval estimates (at 95% confidence level) of the SRD ratios between respective stages. For consistency, two-membrane grana were also omitted. The statistical analysis was performed using SAS 9.4 (SAS Institute, 2013).

The tendency of grana to grow in the vertical or lateral direction was quantified as follows. First, the lateral growth tendency was expressed as a ratio of the lateral growth to the vertical growth during transition between stages. Next, the ratios of these quantities found for the stage 2.0 to 3.3 and the stage 1.8 to 2.0 transitions were calculated. This ratio is a measure of the tendency of the lateral/vertical growth change between the transitions. The interval estimates (at 95% confidence level) of these ratios were found using a simple percentile bootstrap and the standard normal bootstrap (Manly, 1997).

ET

Samples for the ET were cut into 250-nm-thick sections and placed on 100 mesh nickel formvar-coated grids. The electron tomograms were collected with the JEM 1400 electron microscope (Jeol) of the Nencki Institute of the Polish Academy of Sciences, Warsaw, with tomography supply at the voltage of 120 kV. The images were taken at a magnification of 60,000× from +60° to −60° at 1° intervals around one axis. When necessary for alignment, colloidal gold was precipitated onto grids containing thick sections. Forty tomograms from seven developmental stages were collected. Each set of aligned single-axis tomogram tilts was reconstructed using the TomoJ software (component of ImageJ) (Messaoudii et al., 2007). For the reconstruction, 30 iterations of the SIRT algorithm, or 15 iterations of the ART algorithm, were applied (Messaoudii et al., 2007), depending on the quality of the reconstructed image stacks. Tomograms were displayed and analyzed with Imaris software to create the isosurface of the internal plastid membranes. Additionally, the outlines of regions of interest of the tomograms were shaped and analyzed with 3DMOD software (IMOD; Kremer et al., 1996) to reconstruct selected areas of the developing chloroplast membranes. 3D theoretical models of PLB units were created with the help of 3ds max software (Autodesk).

CLSM and 3D Reconstruction

Etioplasts and developing chloroplasts were isolated in a semifrozen 20 mM Tricine-NaOH (pH 7.5) buffer containing 330 mM sorbitol, 40 mM ascorbate, 15 mM NaCl, and 4 mM $MgCl_2$ by gentle homogenization. After filtration, homogenates were centrifuged at 7000*g* for 10 min (first day of experiment) or at 2000*g* for 5 min (second and third day of experiment). Pellets obtained in such a way were very gently resuspended in a small

amount of 20 mM HEPES-NaOH (pH 7.0) buffer containing 330 mM sorbitol, 15 mM NaCl, and 4 mM $MgCl_2$.

Isolated intact chloroplasts were suspended in 20 mM HEPES-NaOH (pH 7.5) containing 330 mM sorbitol, 6% (v/v) glycerol, 15 mM NaCl, and 4 mM $MgCl_2$ to a final chlorophyll concentration of 30 μg mL^{-1}. After 10 min of incubation in the dark and on ice, the suspension was immobilized on a microscope glass covered with poly-L-lysine (Rumak et al., 2010). Chloroplast images from three independent experiments were taken using the Nikon A1 MP confocal laser scanning fluorescence microscope as described previously (Janik et al., 2013). Briefly, the excitation beam was set at 561 nm, and fluorescence emission was recorded in the range of 662 to 737 nm. Fluorescence images of 512 $\times$ 512 pixels were collected from different focal planes (*z* axis step = 25 nm) using a fast resonant scanner with the scanning speed of 15 frames per second, and each optical slice was an average of 16 separate frames. The collected data stacks were subjected to a deconvolution procedure using AutoQuant X3 software (Media Cybernetics) to remove the spherical aberration effect and unspecific fluorescence signals. The deconvolution parameter values were chosen to maximize the image quality, while keeping a minimal data loss, which corresponds to 10 iterations with a medium noise level. The 3D models were created based on the algorithm of the intensity gradient using Imaris 6.3.1 software (Bitplane) (Rumak et al., 2012).

Low-Temperature (77K) Fluorescence Measurements

A modified Cary Eclipse spectrofluorimeter (Varian) with optical fibers guiding the excitation and emission beams was used to record the low temperature (77K) fluorescence emission and excitation spectra. Samples containing preparations of etioplasts or developing chloroplasts were placed in a polytetrafluoroethylene cuvette and subsequently submerged in liquid nitrogen. The emission spectra were recorded in the range of 600 to 800 nm with the wavelength of the excitation beam set at 440 nm. The fluorescence excitation spectra were recorded in the range of 350 to 600 nm, and the emission was set at the center of the main emission bands of the analyzed samples. All spectra were recorded through the LP610 emission filter and the excitation spectra were corrected for the xenon lamp intensity.

Mild Denaturing Electrophoresis

Etioplast/chloroplast membranes were solubilized in a 10 mM Tricine buffer (pH 7.6) containing 20% (w/v) sucrose to a chlorophyll concentration of 0.5 mg mL^{-1}. Next, the *n*-dodecyl-β-D-maltopyranoside and lithium dodecylsulfate were added to a final concentration of 0.5% (w/v) and 0.05% (w/v), respectively. After 20 min of dark incubation on ice, samples containing 4 μg of chlorophyll were loaded into wells of an SDS-depleted 3% (w/v) polyacrylamide stacking gel. Electrophoresis was performed using a SDS-depleted 8% (w/v) polyacrylamide resolving gel supplemented with 10% (w/v) sucrose. The electrophoresis was conducted with a 25 mM Tris buffer (pH 8.3) containing 192 mM glycine and 0.1% (w/v) lithium dodecylsulfate in a MiniProtean3 electrophoresis cell (Bio-Rad Laboratories).

SDS-PAGE and Immunoblot Analysis

Isolated etioplasts/chloroplasts were suspended in Laemmli sample buffer (Bio-Rad Laboratories), and samples containing an equal amount of protein were loaded into polyacrylamide gel wells. After separation by the standard SDS-PAGE, proteins were detected on the PVDF membrane by using primary antibodies against D1, D2, CP43, CP47, Lhcb1, and Lhcb2 (Agrisera) followed by anti-rabbit horseradish peroxidase conjugate and the ECL Detection System (Bio-Rad Laboratories). Primary and secondary antibodies were diluted according to the manufacturers' protocols: Agrisera and Bio-Rad, respectively.

Supplemental Data

Supplemental Figure 1. Scheme of the Experiment.

Supplemental Figure 2. Theoretical Model of the Hexagonal Lattice.

Supplemental Figure 3. Model of the Chlorophyll Fluorescence of Intact Chloroplasts (CLSM) and 3D Reconstruction of Grana Distribution at the 2.0 Developmental Stage.

Supplemental Figure 4. Model of the Chlorophyll Fluorescence of Intact Chloroplasts (CLSM) and 3D Reconstruction of Grana Distribution at the 3.3 Developmental Stage.

Supplemental Figure 5. Distribution of Grana Size in the 1.8, 2.0, and 3.3 Developmental Stages.

Supplemental Table 1. Characterization of the Chloroplast Grana from the 1.8, 2.0, and 3.3 Developmental Stages.

Supplemental Table 2. Ratios of the Geometric Means of GLI for Pairs of Stages, Grana Consisting of Different Number of Membranes (>2) Taken Together.

Supplemental Table 3. Ratios of the Geometric Means of GLI for Pairs of Stages, Calculated Separately for Grana Consisting of a Particular Number of Membranes.

Supplemental Table 4. Ratios of the Geometric Means of SRD for Pairs of Stages, Grana Consisting of Different Number of Membranes (>2) Taken Together.

Supplemental Table 5. Spearman Rank Correlations between the Granum Height and Number of Membranes (When >2) for Subsequent Stages.

Supplemental Table 6. Tendency of Grana for the Lateral or Vertical Enlargement and Its Change in Subsequent Stage-to-Stage Transitions.

The following material has been deposited in the DRYAD repository under accession number http://dx.doi.org/10.5061/dryad.fn203.

Supplemental Movie 1. Video Presenting the Dynamic Model of the Chloroplast Biogenesis Based on the Electron Tomography Reconstructions of Seven Subsequent Developmental Stages and on 2D Theoretical Models.

ACKNOWLEDGMENTS

This work was supported by the Polish Ministry of Science and Higher Education Grant N303 530438. TEM images were performed in the Laboratory of Electron Microscopy, Nencki Institute of Experimental Biology, using a JEM 1400 electron microscope (Jeol). This equipment was installed within the project sponsored by the EU Structural Funds: Centre of Advanced Technology BIM, equipment purchase for the Laboratory of Biological and Medical Imaging. We thank Tomasz Wyszomirski for help with statistical analysis, Wiesław I. Gruszecki for making available the Cary Eclipse spectrofluorimeter, and Piotr Deuar for critical reading of the manuscript.

AUTHOR CONTRIBUTIONS

Ł.K., R.M., A.M., and M.G. designed the research. Ł.K., R.M., and S.S. performed measurements. Ł.K., R.M., and M.G. analyzed data. A.M., Ł.K., R.M., and M.G. wrote the article.

Received December 29, 2015; revised February 16, 2016; accepted March 16, 2016; published March 21, 2016.

REFERENCES

Abdelkader, A.F., Aronsson, H., Solymosi, K., Böddi, B., and Sundqvist, C. (2007). High salt stress induces swollen prothylakoids in dark-grown wheat and alters both prolamellar body transformation and reformation after irradiation. J. Exp. Bot. **58:** 2553–2564.

Abramoff, M.D., Magalhaes, P.J., and Ram, S.J. (2004). Image processing with ImageJ. Biophotonics International. **11:** 36–42.

Adam, Z., Charuvi, D., Tsabari, O., Knopf, R.R., and Reich, Z. (2011). Biogenesis of thylakoid networks in angiosperms: knowns and unknowns. Plant Mol. Biol. **76:** 221–234.

Almsherqi, Z.A., Kohlwein, S.D., and Deng, Y. (2006). Cubic membranes: a legend beyond the Flatland* of cell membrane organization. J. Cell Biol. **173:** 839–844.

Almsherqi, Z.A., Landh, T., Kohlwein, S.D., and Deng, Y. (2009). Chapter 6: cubic membranes the missing dimension of cell membrane organization. Int. Rev. Cell Mol. Biol. **274:** 275–342.

Anderson, J.M., Chow, W.S., and De Las Rivas, J. (2008). Dynamic flexibility in the structure and function of photosystem II in higher plant thylakoid membranes: the grana enigma. Photosynth. Res. **98:** 575–587.

Andrizhiyevskaya, E.G., Chojnicka, A., Bautista, J.A., Diner, B.A., van Grondelle, R., and Dekker, J.P. (2005). Origin of the F685 and F695 fluorescence in photosystem II. Photosynth. Res. **84:** 173–180.

Austin II, J.R., and Staehelin, L.A. (2011). Three-dimensional architecture of grana and stroma thylakoids of higher plants as determined by electron tomography. Plant Physiol. **155:** 1601–1611.

Baena-González, E., and Aro, E.-M. (2002). Biogenesis, assembly and turnover of photosystem II units. Philos. Trans. R. Soc. Lond. B Biol. Sci. **357:** 1451–1459, discussion 1459–1460.

Belcher, S., Williams-Carrier, R., Stiffler, N., and Barkan, A. (2015). Large-scale genetic analysis of chloroplast biogenesis in maize. Biochim. Biophys. Acta **1847:** 1004–1016.

Blomqvist, L.A., Ryberg, M., and Sundqvist, C. (2008). Proteomic analysis of highly purified prolamellar bodies reveals their significance in chloroplast development. Photosynth. Res. **96:** 37–50.

Böddi, B., Kis-Petik, K., Kaposi, A.D., Fidy, J., and Sundqvist, C. (1998). The two spectroscopically different short wavelength protochlorophyllide forms in pea epicotyls are both monomeric. Biochim. Biophys. Acta **1365:** 531–540.

Börner, T., Aleynikova, A.Y., Zubo, Y.O., and Kusnetsov, V.V. (2015). Chloroplast RNA polymerases: Role in chloroplast biogenesis. Biochim. Biophys. Acta **1847:** 761–769.

Casazza, A.P., Szczepaniak, M., Müller, M.G., Zucchelli, G., and Holzwarth, A.R. (2010). Energy transfer processes in the isolated core antenna complexes CP43 and CP47 of photosystem II. Biochim. Biophys. Acta **1797:** 1606–1616.

Charuvi, D., Kiss, V., Nevo, R., Shimoni, E., Adam, Z., and Reich, Z. (2012). Gain and loss of photosynthetic membranes during plastid differentiation in the shoot apex of Arabidopsis. Plant Cell **24:** 1143–1157.

Chong, K., and Deng, Y. (2012). The three dimensionality of cell membranes: lamellar to cubic membrane transition as investigated by electron microscopy. Methods Cell Biol. **108:** 319–343.

Chow, W.S., Kim, E.-H., Horton, P., and Anderson, J.M. (2005). Granal stacking of thylakoid membranes in higher plant chloroplasts: the physicochemical forces at work and the functional consequences that ensue. Photochem. Photobiol. Sci. **4:** 1081–1090.

Dall'Osto, L., Bressan, M., and Bassi, R. (2015). Biogenesis of light harvesting proteins. Biochim. Biophys. Acta **1847:** 861–871.

Danielsson, R., Albertsson, P.-A., Mamedov, F., and Styring, S. (2004). Quantification of photosystem I and II in different parts of the thylakoid membrane from spinach. Biochim. Biophys. Acta **1608:** 53–61.

Danielsson, R., Suorsa, M., Paakkarinen, V., Albertsson, P.-A., Styring, S., Aro, E.-M., and Mamedov, F. (2006). Dimeric and monomeric organization of photosystem II. Distribution of five distinct complexes in the different domains of the thylakoid membrane. J. Biol. Chem. **281:** 14241–14249.

Daum, B., and Kühlbrandt, W. (2011). Electron tomography of plant thylakoid membranes. J. Exp. Bot. **62:** 2393–2402.

Daum, B., Nicastro, D., Austin II, J., McIntosh, J.R., and Kühlbrandt, W. (2010). Arrangement of photosystem II and ATP synthase in chloroplast membranes of spinach and pea. Plant Cell **22:** 1299–1312.

Dekker, J.P., and Boekema, E.J. (2005). Supramolecular organization of thylakoid membrane proteins in green plants. Biochim. Biophys. Acta **1706:** 12–39.

Deng, Y., Almsherqi, Z.A., Ng, M.M.L., and Kohlwein, S.D. (2010). Do viruses subvert cholesterol homeostasis to induce host cubic membranes? Trends Cell Biol. **20:** 371–379.

Deng, Y., Marko, M., Buttle, K.F., Leith, A., Mieczkowski, M., and Mannella, C.A. (1999). Cubic membrane structure in amoeba (*Chaos carolinensis*) mitochondria determined by electron microscopic tomography. J. Struct. Biol. **127:** 231–239.

Deng, Y., and Mieczkowski, M. (1998). Three-dimensional periodic cubic membrane structure in the mitochondria of amoebae *Chaos carolinensis*. Protoplasma **203:** 16–25.

Engel, B.D., Schaffer, M., Kuhn Cuellar, L., Villa, E., Plitzko, J.M., and Baumeister, W. (2015). Native architecture of the Chlamydomonas chloroplast revealed by in situ cryo-electron tomography. eLife **4:** e04889.

Gabruk, M., Stecka, A., Strzałka, W., Kruk, J., Strzałka, K., and Mysliwa-Kurdziel, B. (2015). Photoactive protochlorophyllide-enzyme complexes reconstituted with PORA, PORB and PORC proteins of *A. thaliana*: fluorescence and catalytic properties. PLoS One **10:** e0116990.

Garab, G. (2014). Hierarchical organization and structural flexibility of thylakoid membranes. Biochim. Biophys. Acta **1837:** 481–494.

Garstka, M., Drozak, A., Rosiak, M., Venema, J.H., Kierdaszuk, B., Simeonova, E., van Hasselt, P.R., Dobrucki, J., and Mostowska, A. (2005). Light-dependent reversal of dark-chilling induced changes in chloroplast structure and arrangement of chlorophyll-protein complexes in bean thylakoid membranes. Biochim. Biophys. Acta **1710:** 13–23.

Goral, T.K., Johnson, M.P., Duffy, C.D.P., Brain, A.P.R., Ruban, A.V., and Mullineaux, C.W. (2012). Light-harvesting antenna composition controls the macrostructure and dynamics of thylakoid membranes in Arabidopsis. Plant J. **69:** 289–301.

Grzyb, J.M., Solymosi, K., Strzałka, K., and Mysliwa-Kurdziel, B. (2013). Visualization and characterization of prolamellar bodies with atomic force microscopy. J. Plant Physiol. **170:** 1217–1227.

Gunning, B.E. (2001). Membrane geometry of "open" prolamellar bodies. Protoplasma **215:** 4–15.

Gunning, B.E. (1965). The fine structure of chloroplast stroma following aldehyde osmium-tetroxide fixation. J. Cell Biol. **24:** 79–93.

Gunning, B.E.S., and Steer, M.W. (1975). Ultrastructure and the Biology of Plant Cell. (London: Edward Arnold).

Hasegawa, M., Shiina, T., Terazima, M., and Kumazaki, S. (2010). Selective excitation of photosystems in chloroplasts inside plant leaves observed by near-infrared laser-based fluorescence spectral microscopy. Plant Cell Physiol. **51:** 225–238.

Janik, E., Bednarska, J., Zubik, M., Puzio, M., Luchowski, R., Grudzinski, W., Mazur, R., Garstka, M., Maksymiec, W., Kulik, A., Dietler, G., and Gruszecki, W.I. (2013). Molecular architecture of

plant thylakoids under physiological and light stress conditions: a study of lipid-light-harvesting complex II model membranes. Plant Cell **25:** 2155–2170.

Jarvis, P., and López-Juez, E. (2013). Biogenesis and homeostasis of chloroplasts and other plastids. Nat. Rev. Mol. Cell Biol. **14:** 787–802.

Jensen, P.E., and Leister, D. (2014). Chloroplast evolution, structure and functions. F1000Prime Rep. **6:** 40.

Jia, H., Liggins, J.R., and Chow, W.S. (2014). Entropy and biological systems: experimentally-investigated entropy-driven stacking of plant photosynthetic membranes. Sci. Rep. **4:** 4142.

Kim, E.-H., Chow, W.S., Horton, P., and Anderson, J.M. (2005). Entropy-assisted stacking of thylakoid membranes. Biochim. Biophys. Acta **1708:** 187–195.

Kim, E.-H., Li, X.-P., Razeghifard, R., Anderson, J.M., Niyogi, K.K., Pogson, B.J., and Chow, W.S. (2009). The multiple roles of light-harvesting chlorophyll a/b-protein complexes define structure and optimize function of Arabidopsis chloroplasts: a study using two chlorophyll b-less mutants. Biochim. Biophys. Acta **1787:** 973–984.

Kirchhoff, H., Haase, W., Haferkamp, S., Schott, T., Borinski, M., Kubitscheck, U., and Rögner, M. (2007). Structural and functional self-organization of photosystem II in grana thylakoids. Biochim. Biophys. Acta **1767:** 1180–1188.

Kirchhoff, H., Hall, C., Wood, M., Herbstová, M., Tsabari, O., Nevo, R., Charuvi, D., Shimoni, E., and Reich, Z. (2011). Dynamic control of protein diffusion within the granal thylakoid lumen. Proc. Natl. Acad. Sci. USA **108:** 20248–20253.

Kirchhoff, H., Lenhert, S., Büchel, C., Chi, L., and Nield, J. (2008). Probing the organization of photosystem II in photosynthetic membranes by atomic force microscopy. Biochemistry **47:** 431–440.

Kleffmann, T., von Zychlinski, A., Russenberger, D., Hirsch-Hoffmann, M., Gehrig, P., Gruissem, W., and Baginsky, S. (2007). Proteome dynamics during plastid differentiation in rice. Plant Physiol. **143:** 912–923.

Klein, S., Bryan, G., and Bogorad, L. (1964). Early stages in the development of plastid fine structure in red and far-red light. J. Cell Biol. **22:** 433–442.

Klimmek, F., Ganeteg, U., Ihalainen, J.A., van Roon, H., Jensen, P.E., Scheller, H.V., Dekker, J.P., and Jansson, S. (2005). Structure of the higher plant light harvesting complex I: in vivo characterization and structural interdependence of the Lhca proteins. Biochemistry **44:** 3065–3073.

Kota, Z., Horvath, L.I., Droppa, M., Horvath, G., Farkas, T., and Pali, T. (2002). Protein assembly and heat stability in developing thylakoid membranes during greening. Proc. Natl. Acad. Sci. USA **99:** 12149–12154.

Kouřil, R., Dekker, J.P., and Boekema, E.J. (2012). Supramolecular organization of photosystem II in green plants. Biochim. Biophys. Acta **1817:** 2–12.

Kremer, J.R., Mastronarde, D.N., and McIntosh, J.R. (1996). Computer visualization of three-dimensional image data using IMOD. J. Struct. Biol. **116:** 71–76.

Ling, Q., Huang, W., Baldwin, A., and Jarvis, P. (2012). Chloroplast biogenesis is regulated by direct action of the ubiquitin-proteasome system. Science **338:** 655–659.

Ling, Q., and Jarvis, P. (2015). Functions of plastid protein import and the ubiquitin-proteasome system in plastid development. Biochim. Biophys. Acta **1847:** 939–948.

López-Juez, E. (2007). Plastid biogenesis, between light and shadows. J. Exp. Bot. **58:** 11–26.

Lyska, D., Meierhoff, K., and Westhoff, P. (2013). How to build functional thylakoid membranes: from plastid transcription to protein complex assembly. Planta **237:** 413–428.

Manly, B.F.J. (1997). Randomization, Bootstrap and Monte Carlo Methods in Biology, 2nd ed. (Boca Raton, FL: CRC Press).

Mehta, M., Sarafis, V., and Critchley, C. (1999). Thylakoid membrane architecture. Funct. Plant Biol. **26:** 709–716.

Messaoudii, C., Boudier, T., Sanchez Sorzano, C.O., and Marco, S. (2007). TomoJ: tomography software for three-dimensional reconstruction in transmission electron microscopy. BMC Bioinformatics **8:** 288.

Mostowska, A. (1986a). Changes induced on the prolamellar body of pea seedlings by white, red and blue low intensity light. Protoplasma **131:** 166–173.

Mostowska, A. (1986b). Thylakoid and grana formation during the development of pea chloroplasts, illuminated by white, red, and blue low intensity light. Protoplasma **134:** 88–94.

Mustárdy, L., Buttle, K., Steinbach, G., and Garab, G. (2008). The three-dimensional network of the thylakoid membranes in plants: quasihelical model of the granum-stroma assembly. Plant Cell **20:** 2552–2557.

Mysliwa-Kurdziel, B., Kruk, J., and Strzałka, K. (2013). Protochlorophyllide in model systems–an approach to in vivo conditions. Biophys. Chem. **175-176:** 28–38.

Nevo, R., Charuvi, D., Tsabari, O., and Reich, Z. (2012). Composition, architecture and dynamics of the photosynthetic apparatus in higher plants. Plant J. **70:** 157–176.

Paolillo, D.J., Jr. (1970). The three-dimensional arrangement of intergranal lamellae in chloroplasts. J. Cell Sci. **6:** 243–255.

Park, H., Kreunen, S.S., Cuttriss, A.J., DellaPenna, D., and Pogson, B.J. (2002). Identification of the carotenoid isomerase provides insight into carotenoid biosynthesis, prolamellar body formation, and photomorphogenesis. Plant Cell **14:** 321–332.

Pogson, B.J., and Albrecht, V. (2011). Genetic dissection of chloroplast biogenesis and development: an overview. Plant Physiol. **155:** 1545–1551.

Pogson, B.J., Ganguly, D., and Albrecht-Borth, V. (2015). Insights into chloroplast biogenesis and development. Biochim. Biophys. Acta **1847:** 1017–1024.

Pribil, M., Labs, M., and Leister, D. (2014). Structure and dynamics of thylakoids in land plants. J. Exp. Bot. **65:** 1955–1972.

Rast, A., Heinz, S., and Nickelsen, J. (2015). Biogenesis of thylakoid membranes. Biochim. Biophys. Acta **1847:** 821–830.

Rietveld, A., van Kemenade, T.J., Hak, T., Verkleij, A.J., and de Kruijff, B. (1987). The effect of cytochrome c oxidase on lipid polymorphism of model membranes containing cardiolipin. Eur. J. Biochem. **164:** 137–140.

Rosinski, J., and Rosen, W.G. (1972). Chloroplast development: fine structure and chlorophyll synthesis. Q. Rev. Biol. **47:** 160–191.

Rudowska, L., Gieczewska, K., Mazur, R., Garstka, M., and Mostowska, A. (2012). Chloroplast biogenesis - correlation between structure and function. Biochim. Biophys. Acta **1817:** 1380–1387.

Rumak, I., Gieczewska, K., Kierdaszuk, B., Gruszecki, W.I., Mostowska, A., Mazur, R., and Garstka, M. (2010). 3-D modelling of chloroplast structure under (Mg^{2+}) magnesium ion treatment. Relationship between thylakoid membrane arrangement and stacking. Biochim. Biophys. Acta **1797:** 1736–1748.

Rumak, I., Mazur, R., Gieczewska, K., Kozioł-Lipińska, J., Kierdaszuk, B., Michalski, W.P., Shiell, B.J., Venema, J.H., Vredenberg, W.J., Mostowska, A., and Garstka, M. (2012). Correlation between spatial (3D) structure of pea and bean thylakoid membranes and arrangement of chlorophyll-protein complexes. BMC Plant Biol. **12:** 72.

Ryberg, M., and Sundqvist, C. (1982). Characterization of prolamellar bodies and prothylakoids fractionated from wheat etioplasts. Physiol. Plant. **56:** 125–132.

SAS Institute (2013). SAS/STAT® 12.3 User's Guide. (Cary, NC: SAS Institute).

Schoefs, B., and Franck, F. (2008). The photoenzymatic cycle of NADPH: protochlorophyllide oxidoreductase in primary bean leaves (*Phaseolus vulgaris*) during the first days of photoperiodic growth. Photosynth. Res. **96:** 15–26.

Selstam, E. (1998). Development of thylakoid membranes with respect to lipids. In Lipids in Photosynthesis: Structure, Function and Genetics, S. Paul-André and M. Norio, eds (The Netherlands: Springer), pp. 209–224.

Selstam, E., Schelin, J., Brain, T., and Williams, W.P. (2002). The effects of low pH on the properties of protochlorophyllide oxidoreductase and the organization of prolamellar bodies of maize (*Zea mays*). Eur. J. Biochem. **269:** 2336–2346.

Selstam, E., Schelin, J., Williams, W.P., and Brain, A.P.R. (2007). Structural organisation of prolamellar bodies (PLB) isolated from *Zea mays*. Parallel TEM, SAXS and absorption spectra measurements on samples subjected to freeze-thaw, reduced pH and high-salt perturbation. Biochim. Biophys. Acta **1768:** 2235–2245.

Shimoni, E., Rav-Hon, O., Ohad, I., Brumfeld, V., and Reich, Z. (2005). Three-dimensional organization of higher-plant chloroplast thylakoid membranes revealed by electron tomography. Plant Cell **17:** 2580–2586.

Simidjiev, I., Stoylova, S., Amenitsch, H., Javorfi, T., Mustardy, L., Laggner, P., Holzenburg, A., and Garab, G. (2000). Self-assembly of large, ordered lamellae from non-bilayer lipids and integral membrane proteins in vitro. Proc. Natl. Acad. Sci. USA **97:** 1473–1476.

Solymosi, K., Myśliwa-Kurdziel, B., Bóka, K., Strzałka, K., and Böddi, B. (2006). Disintegration of the prolamellar body structure at high concentrations of Hg^{2+}. Plant Biol (Stuttg) **8:** 627–635.

Solymosi, K., and Schoefs, B. (2010). Etioplast and etio-chloroplast formation under natural conditions: the dark side of chlorophyll biosynthesis in angiosperms. Photosynth. Res. **105:** 143–166.

Solymosi, K., Vitányi, B., Hideg, E., and Böddi, B. (2007). Etiolation symptoms in sunflower (*Helianthus annuus*) cotyledons partially covered by the pericarp of the achene. Ann. Bot. (Lond.) **99:** 857–867.

Standfuss, J., Terwisscha van Scheltinga, A.C., Lamborghini, M., and Kühlbrandt, W. (2005). Mechanisms of photoprotection and nonphotochemical quenching in pea light-harvesting complex at 2.5 A resolution. EMBO J. **24:** 919–928.

Stern, D.B., Hanson, M.R., and Barkan, A. (2004). Genetics and genomics of chloroplast biogenesis: maize as a model system. Trends Plant Sci. **9:** 293–301.

Sun, Y., and Zerges, W. (2015). Translational regulation in chloroplasts for development and homeostasis. Biochim. Biophys. Acta **1847:** 809–820.

Taraschi, T.F., De Kruijff, B., Verkleij, A., and Van Echteld, C.J. (1982). Effect of glycophorin on lipid polymorphism. A 31P-NMR study. Biochim. Biophys. Acta **685:** 153–161.

Tietz, S., et al. (2015). Functional implications of photosystem II crystal formation in photosynthetic membranes. J. Biol. Chem. **290:** 14091–14106.

Vitányi, B., Kósa, A., Solymosi, K., and Böddi, B. (2013). Etioplasts with protochlorophyll and protochlorophyllide forms in the undersoil epicotyl segments of pea (*Pisum sativum*) seedlings grown under natural light conditions. Physiol. Plant. **148:** 307–315.

Vothknecht, U.C., and Westhoff, P. (2001). Biogenesis and origin of thylakoid membranes. Biochim. Biophys. Acta **1541:** 91–101.

Von Wettstein, D., Gough, S., and Kannangara, C.G. (1995). Chlorophyll biosynthesis. Plant Cell **7:** 1039–1057.

von Zychlinski, A., Kleffmann, T., Krishnamurthy, N., Sjölander, K., Baginsky, S., and Gruissem, W. (2005). Proteome analysis of the rice etioplast: metabolic and regulatory networks and novel protein functions. Mol. Cell. Proteomics **4:** 1072–1084.

Waters, M.T., and Langdale, J.A. (2009). The making of a chloroplast. EMBO J. **28:** 2861–2873.

Yang, H., Liu, J., Wen, X., and Lu, C. (2015). Molecular mechanism of photosystem I assembly in oxygenic organisms. Biochim. Biophys. Acta **1847:** 838–848.